

Coupling photocatalysis and piezocatalysis in PVDF/ZnO nanofiber composites for efficient dye degradation

Daud A. Selimov ^{ab*}, Dinara Sobola ^c , Abdulatip Shuaibov ^a ,
Richard Schubert ^c, Rashid Gulakhmedov ^a, Alina Rabadanova ^a ,
Asiyat Magomedova ^a , Farid Orudzhev ^{ab*} 

a: Smart Materials laboratory, Dagestan State University, Makhachkala 367000, Russia
b: Amirkhanov Institute of Physics, Dagestan Federal Research Center, Russian Academy of Sciences, Makhachkala 367003, Russia
c: Department of Physics, Faculty of Electrical Engineering and Communication, Brno University of Technology, Brno 616 00, Czech Republic
* Corresponding author: daud-selimov@live.com, farid-stkha@mail.ru



Abstract

The development of advanced catalytic materials for environmental applications remains a critical challenge due to the limitations of conventional photocatalysis, such as low charge separation efficiency and dependence on external light sources. In this study, we present the synthesis and investigation of electrospun polyvinylidene fluoride (PVDF) nanofibers modified with zinc oxide (ZnO) nanoparticles for enhanced photocatalytic, piezocatalytic, and piezophotocatalytic activity. The morphology and structural properties of the composite material were analyzed using scanning electron microscopy (SEM), energy-dispersive X-ray spectroscopy (EDX), Raman spectroscopy, Fourier-transform infrared (FTIR) spectroscopy, and X-ray photoelectron spectroscopy (XPS). The results show that the incorporation of ZnO reduces the average fiber diameter by 3.3 times and decreases the β -phase fraction from 87.3% to 71.6% due to nanoparticle agglomeration. The catalytic performance of PVDF/ZnO was evaluated in the degradation of methylene blue (MB) under different conditions: photocatalysis (71%), piezocatalysis (76%), and piezophotocatalysis (91%) within 60 minutes. Additionally, the membrane generated an average open-circuit voltage of 140 mV under mechanical stirring, demonstrating its ability to convert mechanical energy into electrical energy. These findings highlight the potential of PVDF/ZnO nanocomposites as multifunctional materials for sustainable catalytic applications and energy harvesting.

Key findings

- Modification of PVDF with ZnO nanoparticles reduced fiber diameter by 3.3 times and decreased β -phase content from 87.3% to 71.6%.
- The PVDF/ZnO composite demonstrated high catalytic efficiency: 71% (photocatalysis), 76% (piezocatalysis), and 91% (piezophotocatalysis) for methylene blue degradation within 60 min.
- Under mechanical stirring, PVDF/ZnO achieved 85% methylene blue degradation via piezophotocatalysis, indicating efficient charge separation and catalytic enhancement.
- The PVDF/ZnO membrane generated a stable open-circuit voltage of \sim 140 mV under mechanical stimulation, confirming its piezoelectric properties.

© 2025, the Authors. This article is published in open access under the terms and conditions of the Creative Commons Attribution (CC BY) license (<http://creativecommons.org/licenses/by/4.0/>).

1. Introduction

In recent years, the issue of environmental pollution has gained significant global attention due to the rapid

development of industry and the widespread use of chemical and biological reagents. Photocatalytic degradation is considered one of the most promising technologies for addressing environmental challenges, particularly in the

Accompanying information

Article history

Received: 21.03.25
Revised: 14.04.25
Accepted: 17.04.25
Available online: 27.04.25

Keywords

PVDF; ZnO; photocatalysis; piezocatalysis; piezophotocatalysis; electrospinning

Funding

This work was supported by the Russian Science Foundation (grant no. 22-73-10092) <https://www.rscf.ru/project/22-73-10091/>.

Supplementary information

Transparent peer review: 

Sustainable Development Goals



context of wastewater treatment. Solar energy, as a clean and renewable resource, enables the decomposition of organic pollutants in aqueous solutions into non-toxic molecules [1]. However, its practical application remains limited, primarily due to the low photocatalytic activity, which is largely attributed to the high recombination rate of photogenerated charge carriers. In recent years, the utilization of piezoelectric materials in photocatalytic processes has emerged as a popular solution [2–4]. Among the most well-known and extensively studied piezoelectric materials are BaTiO₃ [5], NaNbO₃ [6], BiFeO₃ [7], ZnSnO₃ [8], MoS₂ [9], CdS [10], ZnS [11], and ZnO [12].

Zinc oxide (ZnO) is a direct wide-bandgap semiconductor with a bandgap energy of 3.37 eV, characterized by a wurtzite crystal structure and a high piezoelectric coefficient [13, 14]. Specifically, in the study [15], the piezocatalytic oxidation of Acid Orange 7 (AO7) at a concentration of 5 μM was thoroughly investigated using ZnO nanorods. The results demonstrated an oxidation efficiency of 80% within 50 minutes, establishing that the oxidation process occurs with the involvement of hydroxyl radicals (•OH). The piezocatalytic properties of ZnO were also explored in several other studies [16–19].

Dispersed heterogeneous piezocatalysts exhibit several critical drawbacks, including brittleness, high cost, complexity of manufacturing, and potential sources of secondary pollution. Given these limitations, organic piezocatalysts represent a more promising research direction, with polyvinylidene fluoride (PVDF) holding a particularly important position. This material offers several advantages, such as environmental safety, biocompatibility, flexibility, and high resistance to halogens and acids [20]. PVDF is characterized by a semicrystalline structure and exists in five polymorphic modifications: α, β, γ, δ, and ε. The piezoelectric properties of this polymer are attributed to the presence of the polar β-phase (TG TG') and the partially polar γ-phase (T₃GT₃G'). Notably, the β-phase makes a significant contribution to the piezoelectric characteristics due to its more pronounced dipole moment. Previous studies investigated the catalytic properties of PVDF-based composites with zinc oxide. For instance, in one study [21], the high efficiency of rhodamine B dye degradation was demonstrated, reaching 88% within 60 minutes, along with confirmation of the composite's stability in acidic and alkaline environments. Additionally, another study [22] demonstrated that a PVDF composite film modified with ZnO nanotetrapods exhibited outstanding results in the piezophotocatalytic degradation of methylene blue and azithromycin, achieving degradation levels of 96.0% and 92.6%, respectively, within 25 and 60 min. The incorporation of PVDF/T-ZnO led to an approximately 40% increase in the degradation rate of organic molecules compared to the use of pure ZnO nanoparticles.

Hence, the aim of this work was to synthesize PVDF/ZnO polymer nanocomposites with both photocatalytic and piezocatalytic properties by electrospinning and to analyze

their catalytic activity in the degradation of the model dye methylene blue. The relationship between the structural-phase composition and morphology of the composite and their catalytic properties was studied. It was shown that the addition of zinc oxide leads to phase changes, in particular, to a decrease in the beta phase. The study of thermal properties showed high thermal stability.

2. Methodology

2.1. Synthesis of PVDF/ZnO

The synthesis of the composite material was carried out using the electrospinning method, which involved the preparation of a 15 wt.% PVDF solution. This was achieved by dissolving PVDF powder (Sigma Aldrich, St. Louis, Michigan, USA, $M_w = 275,000 \text{ g}\cdot\text{mol}^{-1}$) in a mixture of dimethyl sulfoxide (Sigma Aldrich, St. Louis, Michigan, USA) and acetone (Sigma Aldrich, St. Louis, Michigan, USA) at a volumetric ratio of 7:3. Zinc oxide (Sigma Aldrich CAS: 1314-13-2, $D < 100 \text{ nm}$) powder was added at a concentration of 20 wt.% relative to the solution mass. The resulting solution was heated in an ultrasonic bath at 50 °C until complete polymer dissolution and homogenization, which took approximately 1 hour. The prepared solution was then loaded into a syringe with a needle diameter of 1.067 mm (17 G) and subjected to electrospinning under a constant voltage of 50 kV using a 4-SPIN apparatus (Contipro, Dolní Dobrouch, Czech Republic) for 30 minutes at a feed rate of 30 μL·min⁻¹. The obtained fibers were collected on a rotating collector covered with aluminum foil, rotating at a speed of 2000 rpm, with a fixed distance of 20 cm between the needle tip and the collector. The resulting nonwoven fibrous mats were left to dry overnight at room temperature. In the final dried membrane, the PVDF/ZnO mass ratio was 43/67 wt.%.

2.2. Characterization and analysis

The morphology of the samples was analyzed using a scanning electron microscope (SEM) LYRA3 (Tescan, Brno, Czech Republic) equipped with an X-Max 50 EDS detector (Oxford Instruments, Abingdon, UK) and a Helios NanoLab 660 (ThermoFisher Scientific, Brno, Czech Republic). The samples were coated with a thin layer of gold using a Leica EM ACE600 coating device (Leica Microsystems, Wetzlar, Germany).

Raman spectroscopy was performed using a WITec alpha300 R (WITec, Ulm, Germany) with an excitation laser wavelength of 532 nm. The laser power varied from 0.5 mW to 1 mW depending on the sample. The resulting signal was obtained by averaging 50 accumulations with an integration time of 20 s.

FTIR measurements were conducted in transmission mode using a Bruker spectrometer (Billerica, Massachusetts, USA) with a resolution of 1 cm⁻¹ and 512 iterations.

Differential scanning calorimetry (DSC) measurements were performed on DSC 204 F1 (NETZSCH) at a heating and

cooling rate of 10 °C/min, from 25 °C to 200 °C under an argon flux of 100 ml/min.

XPS spectra were recorded using an AXIS Supra™ X-ray photoelectron spectrometer (Kratos Analytical Ltd., Manchester, UK) with an emission current of approximately 15 mA. The spectra were processed using CasaXPS software v.2.3.23.

The device for the piezophotocatalytic degradation study consists of a multilayer structure in which a PVDF/ZnO film (3×1 cm²), serving as the active piezoelectric component, was placed between upper and lower copper foil (Cu) electrodes and tightly laminated in PET for sealing and to eliminate triboelectric effects. Conductive Cu leads were attached to both sides of the electrodes.

The piezophotocatalytic degradation experiments were conducted using UV-visible radiation and an ultrasonic bath with a power of 250 W at a frequency of 18 kHz. A high-pressure mercury lamp (250 W, Philips) was used as the light source in the UV-visible range. To eliminate the influence of temperature on the degradation efficiency, a constant reactor temperature of 26 °C was maintained. Before testing, a film (3×1 cm²) was immersed in a beaker containing a methylene blue (MB) solution (2.5 mg/L, 20 mL) and kept in the dark for 30 minutes to establish adsorption-desorption equilibrium. During the test, 3 mL of the solution was sampled at regular intervals and analyzed using a UV-visible spectrometer. The concentration of the MB dye was measured at its maximum absorption peak at $\lambda = 663$ nm. The degradation percentage was defined as C/C_0 , where C and C_0 represent the measured and initial concentrations of the dye solution, respectively.

3. Results and Discussions

Figure 1 presents the results of the morphological analysis of the membranes obtained by the electrospinning method, along with fiber diameter distribution histograms for pure PVDF and composite PVDF/ZnO.

The SEM image of the pure PVDF membrane (Figure 1a) reveals a smooth and uniform fiber structure without visible defects, whereas after ZnO modification (Figure 1b), the fibers acquire a rough surface, indicating the presence of nanoparticles distributed along their length. The inset in the upper right corner of Figure 1b shows a magnified fragment of the fiber surface, where nanoparticle agglomeration can be observed.

A change in fiber diameter distribution is also evident, as confirmed by the histograms (Figures 1c and 1d). In the case of pure PVDF, the average fiber diameter is approximately 1000 nm, with the majority of fibers falling within the 750–1250 nm range, exhibiting an asymmetric distribution. The addition of ZnO leads to a significant reduction in fiber size to 300–500 nm and a narrowing of the distribution range, which can be attributed to changes in solution viscosity and electrical conductivity upon nanoparticle incorporation.

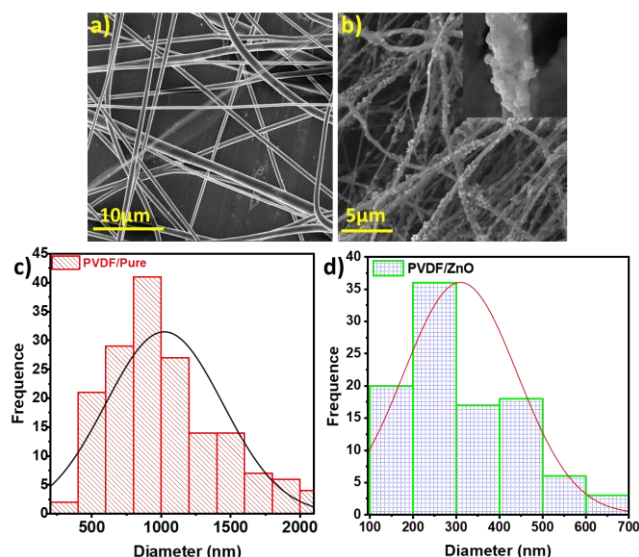


Figure 1 SEM images of the pure and ZnO-doped PVDF membrane (a, b); Fiber diameter distribution histograms (c, d).

Additionally, the characteristic surface roughness induced by ZnO increases the active surface area of the material, potentially enhancing its catalytic activity. The narrower diameter distribution in the composite membrane indicates improved structural uniformity.

The chemical composition analysis of the membranes was conducted using energy-dispersive spectroscopy (EDS) with an energy-dispersive attachment to a scanning electron microscope (SEM). This analysis identifying the key elements within the sample structures (Figure 2a, b). Three specific areas were selected for examination: regions A and B, which exhibited significant particle agglomeration, and region C, representing a nanofiber area unaffected by deformation.

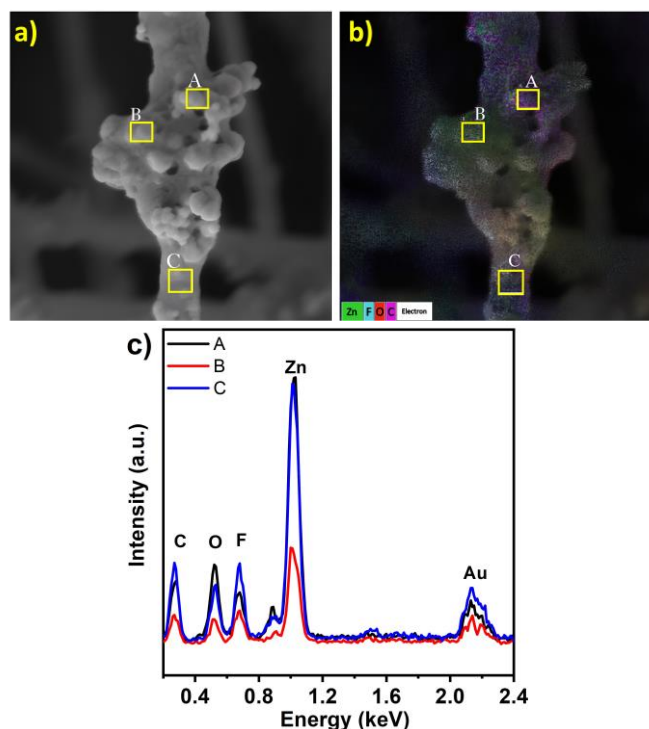


Figure 2 SEM images of the obtained samples (View field 3 μ m) (a); EDS spectra of PVDF/ZnO for regions A, B, and C (b).

The EDS spectra (Figure 2c) confirmed the presence of carbon (C), oxygen (O), fluorine (F), and zinc (Zn) in all examined regions. The detection of Zn in each of the three areas indicates the uniform distribution of zinc oxide along the fibers, both in the agglomerated regions and in structurally intact areas.

Figure 3a presents the Raman scattering spectra of ZnO, demonstrating the characteristic vibrational modes associated with the wurtzite crystal structure. In particular, the peak at 204 cm^{-1} corresponds to the second-order phonon mode $2E_2(\text{low})$ [23], while the most intense polarized mode, $E_2(\text{high})$, appears at 440 cm^{-1} , which is a typical feature of the wurtzite structure [24, 25].

The high intensity of the $E_2(\text{high})$ mode indicates a high degree of ZnO crystallinity. Additionally, first-order transverse optical modes $A_1(\text{TO})$, observed as peaks at 336 cm^{-1} and 382 cm^{-1} , are associated with surface atom disordering in ZnO [26]. An additional peak at 490 cm^{-1} is attributed to surface optical (SO) phonon modes [27, 28]. The low intensity of the peak at 581 cm^{-1} , identified as the $E_1(\text{LO})$ mode, which is linked to Zn interstitials and oxygen defects, indicates a low concentration of point defects in the ZnO crystal lattice [29]. The high-frequency modes $2(\text{LO})$ and $2A_1(\text{LO})$, observed at 1101 cm^{-1} and 1150 cm^{-1} , respectively, are consistent with the literature data [30].

In the Raman scattering spectrum of the PVDF/ZnO composite (Figure 3b), a significant enhancement in the intensity of the surface optical (SO) mode is observed. According to the study [31], this phenomenon is attributed to dielectric effects occurring at the interface between ZnO and the

organic polymer phase. These results are also consistent with findings from [32], where the interfacial contact between Cu and ZnO was investigated, confirming the influence of interphase interactions on the optical properties of the system.

The Raman spectrum of the PVDF/ZnO composite exhibits several bands corresponding to different crystalline modifications of polyvinylidene fluoride (PVDF). The peak at 609 cm^{-1} is identified as a characteristic mode of the α -phase, associated with CF_2 scissoring vibrations and C-C-C skeletal deformation vibrations. Analysis of the $790\text{--}855\text{ cm}^{-1}$ region indicates the predominance of the ferroelectric β -phase, along with partial presence of the γ -phase. The mode at 838 cm^{-1} is associated with CH_2 rocking vibrations and asymmetric CF_2 stretching, which are characteristic of the β -phase [33]. The mode at 810 cm^{-1} indicates the presence of the γ -phase and corresponds to CH_2 out-of-plane wagging. The mode at 800 cm^{-1} is attributed to the paraelectric α -phase and manifests as CH_2 rocking vibrations. In the 881 cm^{-1} region, modes characteristic of the α -, β -, and γ -phases are present, resulting from the symmetric stretching of C-C and CF_2 bonds [34].

Due to the close proximity of peaks corresponding to different crystalline phases, their quantitative assessment using Raman scattering is challenging. To provide a more detailed analysis of the phase composition, additional measurements were performed using Fourier-transform infrared (FTIR) spectroscopy, with the results presented in Figure 4.

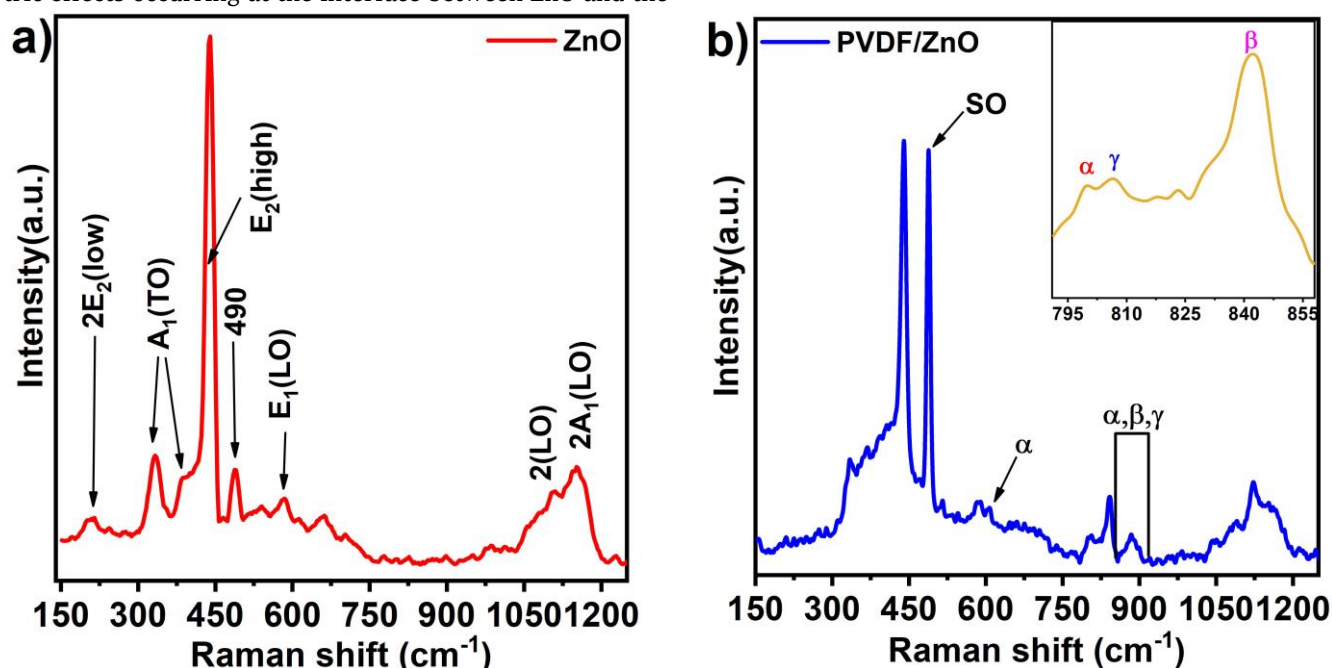


Figure 3 Raman scattering spectra of ZnO nanoparticles (a) and the PVDF/ZnO composite (b).

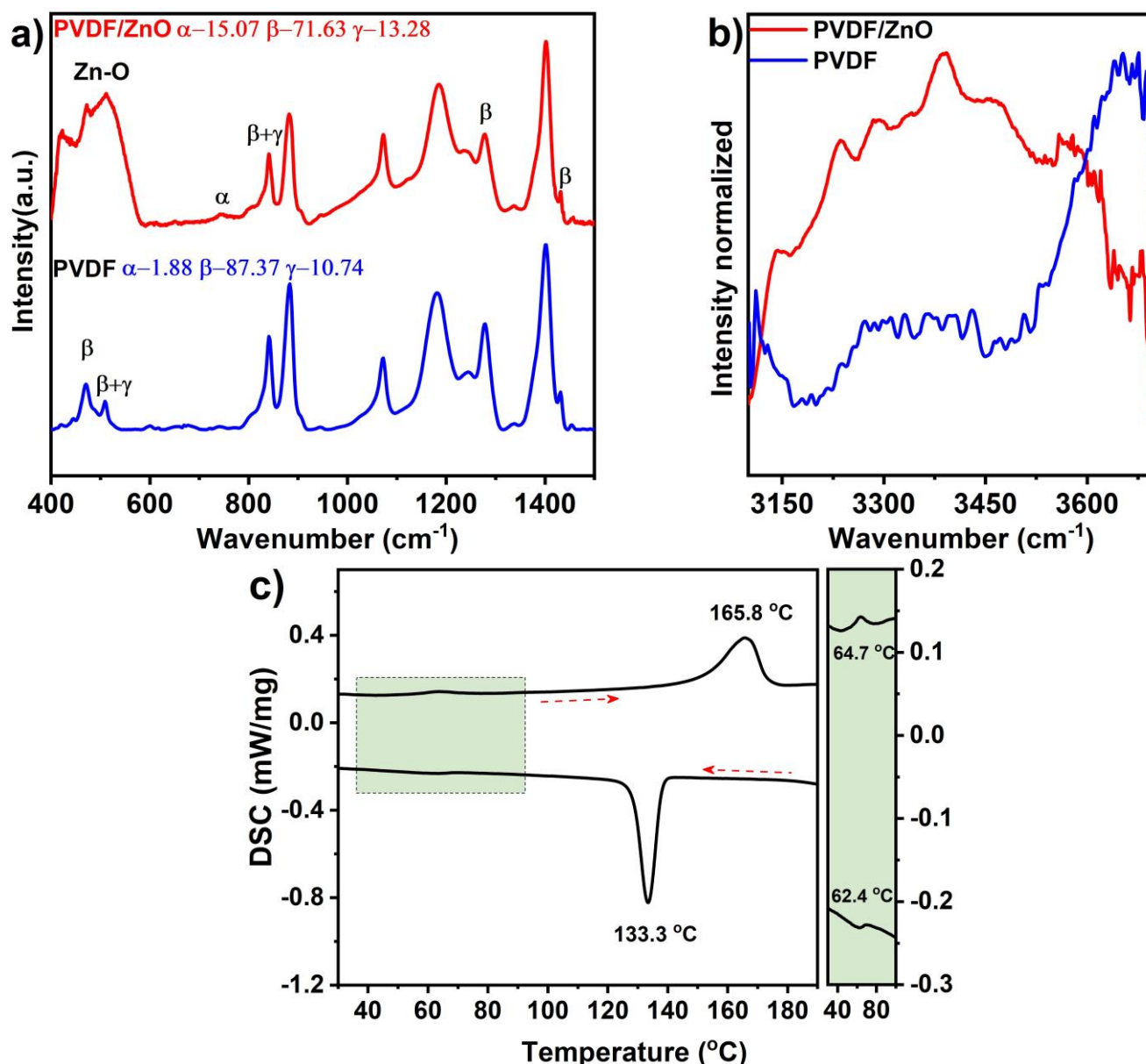


Figure 4 FTIR spectra of pure PVDF and PVDF/ZnO d in the region of 400–1500 cm^{-1} (a) and in the region of 3100–3700 cm^{-1} (b). DSC heating/cooling scans for PVDF/ZnO (c).

For the quantitative analysis of the relative content of α -, β -, and γ -phases in the PVDF/ZnO samples, FTIR spectroscopy spectra were used. The fraction of the electroactive phase ($\beta + \gamma$) was calculated using the formula (1):

$$F_{EA} = \frac{I_{EA}}{\left(\frac{K_{840^*}}{K_{763}}\right) I_{763} + I_{EA}} \cdot 100\%, \quad (1)$$

where I_{EA} and I_{763} represent the absorption intensities at 840* cm^{-1} and 763 cm^{-1} , respectively; K_{840^*} and K_{763} are the absorption coefficients at the corresponding wavenumbers, with the values of $7.7 \cdot 10^4$ and $6.1 \cdot 10^4 \text{ cm}^2 \text{ mol}^{-1}$, respectively.

After determining the fraction of the electroactive phase, the relative content of β - and γ -phases was calculated using the following expressions (2, 3):

$$F(\beta) = F_{EA} \cdot \left(\frac{\Delta H_{\beta'}}{\Delta H_{\beta'} + \Delta H_{\gamma'}}\right) \cdot 100\%, \quad (2)$$

$$F(\gamma) = F_{EA} \cdot \left(\frac{\Delta H_{\gamma'}}{\Delta H_{\beta'} + \Delta H_{\gamma'}}\right) \cdot 100\%, \quad (3)$$

where $\Delta H_{\beta'}$ and $\Delta H_{\gamma'}$ represent the peak height differences (absorption differences) between the peaks at approximately 1275 cm^{-1} and the nearest valley around 1260 cm^{-1} , as well as the peak at 1234 cm^{-1} and the nearest valley around 1225 cm^{-1} , respectively.

The calculations revealed that in pure PVDF, the fraction of the α -phase was 1.88%, the γ -phase was 10.74%, and the β -phase was 87.37%. Upon the addition of ZnO, phase transformations occurred, specifically an increase in the α - and γ -phases to 15.07% and 13.28%, respectively, as well as a decrease in the β -phase fraction to 71.63%. The reduction in the electroactive phase fraction is attributed to the high ZnO particle content, which reduces the β -phase fraction due to its tendency to agglomerate, leading to proportionally fewer nucleation sites for the electroactive phase

per filler particle [35, 36]. This conclusion is further supported by SEM and EDX results.

Figure 4b presents the spectral region of 3100–3700 cm^{-1} , where peaks corresponding to hydroxyl (-OH) group vibrations are observed. In pure PVDF, a narrow peak at 3600 cm^{-1} is detected, indicating the presence of free hydroxyl groups [37]. In the PVDF/ZnO composite sample, a broad asymmetric peak is observed, which is characteristic of various types of intra- and intermolecular hydrogen bonds [38].

Differential scanning calorimetry (DSC) analysis was performed for each PVDF sample to investigate their thermal response and to calculate overall crystallinity. Figure 4c shows the heating and cooling thermograms of the composite material.

The data analysis indicates that the sample exhibits a broad asymmetric melting peak with a maximum at $T_m \approx 165.8$ °C, corresponding to the melting temperature of crystalline phases. According to the previously published

studies, melting peaks in this temperature range can be associated with the α - and β -phases of the polymer [39]. The endothermic peak observed between 40 and 80 °C (inset on the right of Figure 4c) was attributed to the melting of poorly formed secondary crystals, which can be considered as small crystalline domains within the amorphous phase. The crystallinity of the sample, calculated based on the enthalpy of fusion (21.5 J/g), was determined to be 47.9%. The relatively low crystallinity value is attributed to the high filler content, which restricts crystallization processes.

To further investigate the chemical composition of PVDF/ZnO membranes, X-ray photoelectron spectroscopy (XPS) analysis was conducted. The survey spectrum (Figure 5a) of the composite sample identified only chemical states corresponding to C, F, O, and Zn, indicating the chemical purity of the sample. Deconvolution analysis of the C1s peak allowed the identification of different chemical states of carbon.

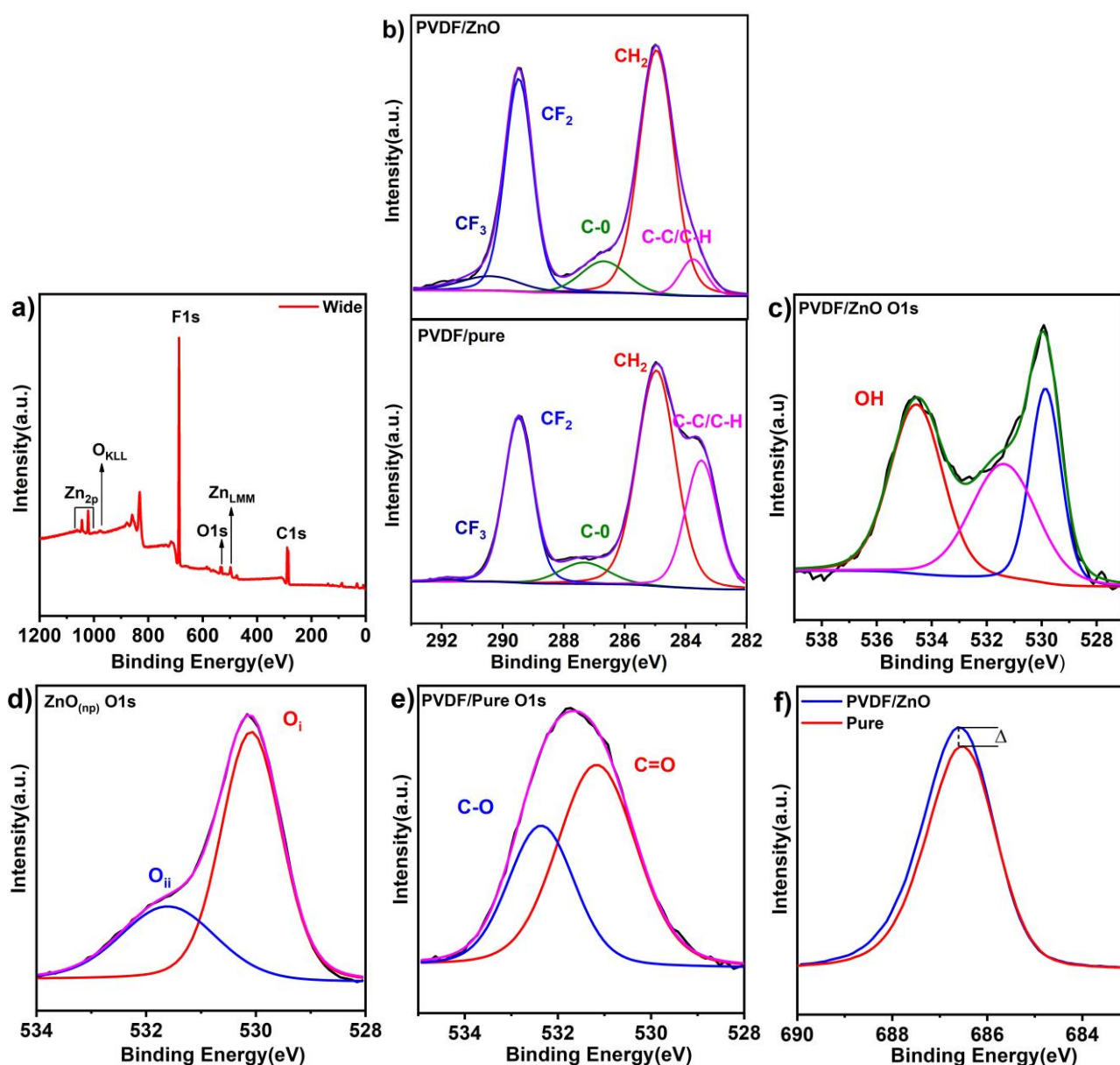


Figure 5 XPS spectra of the sample: survey XPS spectrum (a), detailed C1s peak (b), detailed O1s peak of PVDF/ZnO (c), detailed O1s peak of ZnO (d), detailed O1s peak of pure PVDF (e), detailed F1s peak (f).

The deconvolution of the C1s spectrum revealed that it consists of five components corresponding to different chemical bonds: C-C/C-H (283.4 eV), CH₂ (284.9 eV), C-O (287.3 eV), CF₂ (289.4 eV), and CF₃ (291.7 eV)[40]. Significant changes were observed in the spectrum of the composite sample, including a sharp decrease in the intensity of the C-C/C-H peak, indicating the cleavage of hydrocarbon bonds, and a noticeable increase in the intensity of the CF₃ peak, suggesting an increased concentration of trifluorinated groups. These changes are attributed to the influence of ZnO particles on the crystallization process of PVDF. The spatial volume of nanoparticles hinders the close packing of reactive atoms within the polymer chain, slowing down the crystallization process and leading to structural disruptions. As a result, the breaking of C-C/C-H bonds and the formation of CF₃ groups at the polymer chain ends are observed. Thus, XPS analysis confirms the effect of ZnO on the chemical and structural properties of the polymer, which aligns with the phase analysis results.

Additionally, the O1s spectrum was examined, revealing a complex distribution of oxygen states. The variation in the intensity of C-O components is due to overlapping contributions from different chemical states of oxygen. This is supported by a comparative analysis of the O1s spectra of pure ZnO and PVDF, where the appearance of an additional peak associated with hydroxyl (-OH) groups was also observed (Figure 5c). These hydroxyl groups were previously identified in the 3100–3700 cm⁻¹ region of the IR spectra (Figure 4b).

The O1s spectrum of the pristine ZnO powder (Figure 5d), analyzed using Gaussian fitting, consists of two components: O_i (oxidized O²⁻ ions within the ZnO structure) and O_{ii} (associated with oxygen vacancies or chemisorbed and dissociated oxygen species on the ZnO surface) [41–44]. For pure PVDF, the O1s spectrum (Figure 5e) also consists of two components: C-O (532.4 eV) and C=O (531.2 eV) [38].

The analysis of the F1s spectrum of the composite sample, compared to pure PVDF (Figure 5f), revealed an increase in peak intensity and asymmetry upon the addition of ZnO. This can be attributed to two main factors. First, the increase in CF₃-group concentration leads to a higher fluorine atom density per unit area, thereby increasing the number of electrons susceptible to ionization. Second, changes in the local chemical environment of fluorine atoms occur due to the presence of ZnO nanoparticles and hydroxyl groups. These results confirm the influence of ZnO on the chemical modification of the PVDF polymer matrix, correlating with the observed changes in phase composition and molecular interactions.

The catalytic activity of the PVDF/ZnO composite material was investigated in the degradation of methylene blue (MB) under light irradiation and ultrasonic (US) treatment in the presence of the catalyst. To eliminate the effects of MB degradation due to light and ultrasound alone, control experiments were conducted without the catalyst (sonolysis and photolysis).

The experimental results (Figure 6a) showed that the efficiency of sonolysis reached 52%, while the photolysis degree increased to 62% after 60 minutes of exposure. Under combined catalyst and light conditions (photocatalysis), the photodegradation level increased to 71%. The efficiency of piezocatalytic degradation in the dark reached 76%.

The mechanism of piezocatalysis is based on ultrasonic vibration, which generates a large number of cavitation bubbles. Upon collapse, these bubbles create localized "hot spots" and high pressure, producing shock waves that induce micro-deformations in the composite polymer. These deformations initiate the piezoelectric polarization mechanism in both the polymer itself and the embedded ZnO, which is also a piezoelectric material.

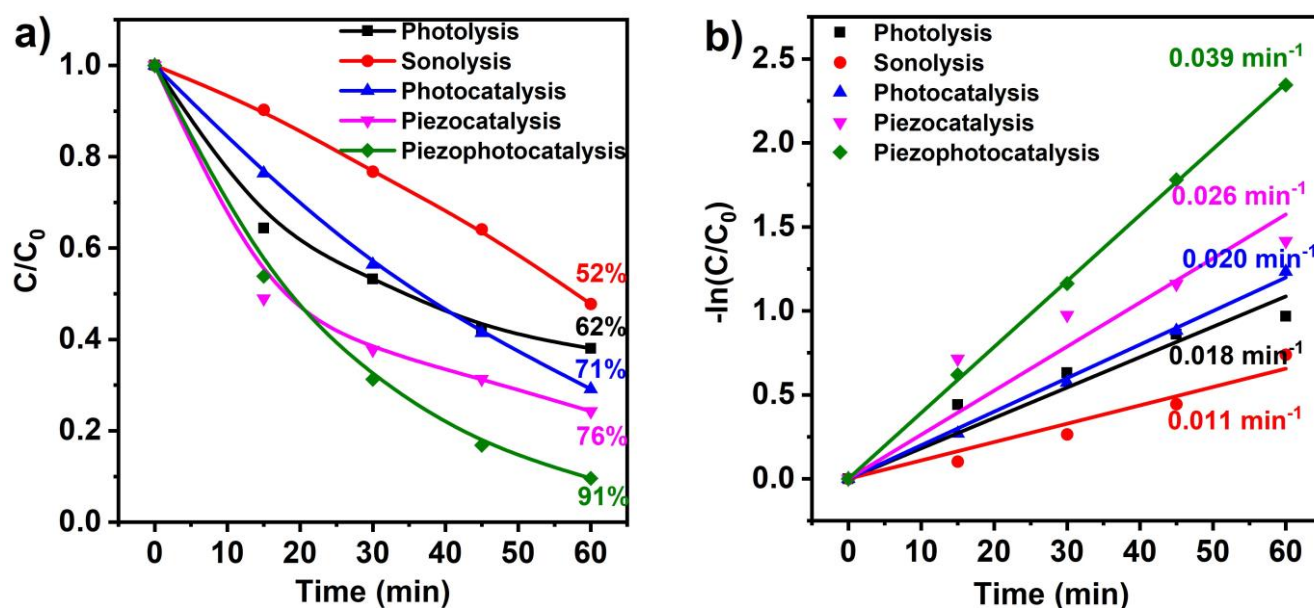


Figure 6 Catalytic activity of the composite in various processes (a) and pseudo-first-order kinetic curves (b).

The literature discusses two primary mechanisms of piezocatalysis. The first is the energy band theory, analogous to photocatalysis, where the piezopotential serves as the driving force for charge transfer to the material's surface, initiating catalytic reactions. In photocatalysis, absorbed photons generate electron-hole pairs that contribute to the formation of reactive oxygen species. In piezocatalysis, the primary source of reactive charge carriers is mechanical excitation, where ultrasonic treatment can directly excite electrons from the valence band (VB) to the conduction band (CB) [45–47].

The second mechanism is the shielding charge effect, which differs from the energy band theory in that the charges involved in redox reactions originate from surface-adsorbed carriers in the external environment rather than from internal charge carriers of the material. In the initial state, the material's surface is electrostatically neutral, but when subjected to external mechanical stress, the density of bound charges changes, leading to the movement of shielding charges and their interaction with water. This interaction results in the formation of reactive oxygen species, such as $\cdot\text{OH}$ and $\cdot\text{O}_2^-$ [48]. The process continues until a new electrostatic equilibrium is reached.

The piezophotocatalytic activity of PVDF/ZnO reached 91%, significantly exceeding the efficiency of individual photocatalysis and piezocatalysis processes due to the synergistic effect. The piezoelectric field generated by ultrasound facilitates the excitation and migration of electron-hole pairs while preventing their recombination, thereby enhancing the material's photocatalytic activity.

The rate constants were calculated using the semi-logarithmic pseudo-first-order equation (4):

$$\ln C/C_0 = kt. \quad (4)$$

The rate constant (k) values were determined to be 0.018, 0.011, 0.020, 0.026, and 0.039 min^{-1} for photolysis, sonolysis, photocatalysis, piezocatalysis, and piezophotocatalysis, respectively. The reaction rate of piezophotocatalysis increased by factors of 2.16, 3.6, 1.9, and 1.5 compared to photolysis, sonolysis, photocatalysis, and piezocatalysis, respectively.

Although the simultaneous combination of ultrasonic vibration and light has been shown to achieve high piezophotocatalytic activity, the practical application of this technology presents a significant challenge due to the limited availability of natural sources of ultrasonic excitation. However, the mechanical energy of water flow in natural environments can potentially be utilized to generate a piezoelectric field. In this regard, piezo- and piezophotocatalytic experiments were conducted using magnetic stirring, with the results presented in Figure 7.

According to the obtained data, the degradation efficiency of MB under simple magnetic stirring without UV irradiation reached 20% after 60 min. Meanwhile, when combining magnetic stirring with UV irradiation, the photodegradation efficiency increased to 85%.

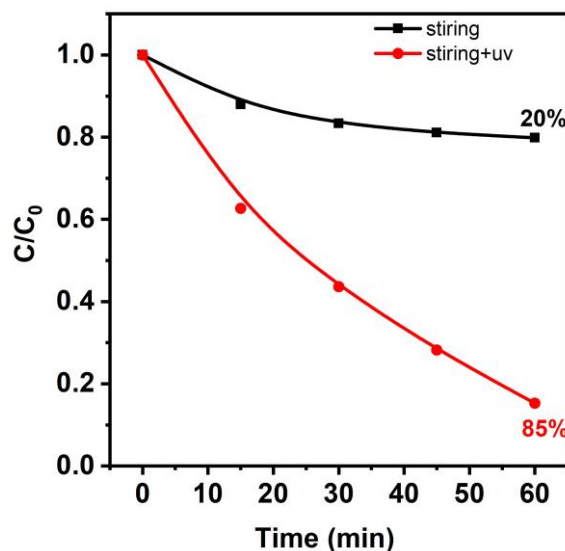


Figure 7 Piezocatalysis and piezophotocatalysis are facilitated by hydrodynamic stirring at a constant speed of 200 rpm.

The mechanical energy generated by water flow induces an electric potential in the piezoelectric material, confirming its applicability in piezocatalytic processes without the need for an external ultrasonic source. This approach highlights the potential of utilizing natural hydrodynamic processes to generate electrical charges capable of initiating catalytic reactions.

To experimentally confirm the ability to convert mechanical energy from water flow into electricity, a piezoelectric nanogenerator (PENG) was assembled using the PVDF/ZnO composite material. Figure 8 illustrates the schematic structure of the PVDF/ZnO-based PENG.

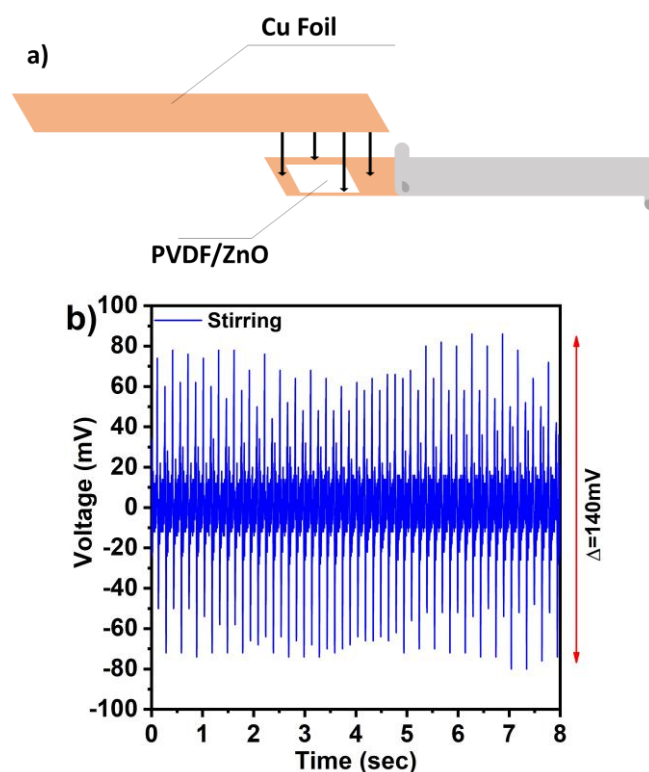


Figure 8 Schematic structure of the piezoelectric nanogenerator (PENG) based on PVDF/ZnO (a); Voltage versus time dependence under mechanical stimulation induced by stirring (b).

To evaluate the generated potential under mechanical excitation, open-circuit voltage measurements were conducted at a fixed stirring speed of 200 rpm using an overhead stirrer. As shown in Figure 8b, the device generates an alternating voltage with a peak-to-peak amplitude of approximately 140 mV, indicating the stable and reproducible operation of the piezoelectric nanogenerator. Continuous mechanical stimulation induces an alternating internal electric field, facilitating the efficient transfer of charges at the PVDF/ZnO-solution interface. This, in turn, may play a crucial role in initiating piezocatalytic processes.

4. Limitations

In the present study, we investigated a PVDF/ZnO composite with a high content of inorganic nanoparticles, where the weight fraction of ZnO (67 wt.%) significantly exceeded that of the polymer matrix. While this composition demonstrated promising photocatalytic and piezocatalytic performance, the high nanoparticle content led to pronounced agglomeration, which in turn reduced the electroactive β -phase content and overall crystallinity. This agglomeration may limit the reproducibility and scalability of the material, as well as its mechanical integrity.

Moreover, the current work focused primarily on structural, morphological, and catalytic properties of the composite. However, a comprehensive evaluation of its optical and piezoelectric properties was beyond the scope of this research. These characteristics are critical for understanding the fundamental mechanisms of charge generation and transfer in piezophotocatalytic systems.

In future studies, we will investigate a broader range of ZnO-to-PVDF ratios in order to optimize the balance between catalytic activity and material stability. We also plan to perform an in-depth analysis of the composite's optical absorption properties, along with a quantitative assessment of its piezoelectric coefficients. These investigations will provide deeper insights into the multifunctional behavior of the material and support its potential integration into self-powered environmental remediation technologies.

5. Conclusion

In this study, PVDF/ZnO nanocomposite membranes were successfully synthesized via electrospinning and systematically investigated for their structural, electrical, and catalytic properties. The incorporation of ZnO nanoparticles significantly altered the morphology and crystalline phases of PVDF, leading to a decrease in fiber diameter and β -phase content. The catalytic experiments demonstrated that the PVDF/ZnO composite exhibits high photocatalytic, piezocatalytic, and piezophotocatalytic activity, achieving 71%, 76%, and 91% degradation of methylene blue, respectively. Furthermore, the ability of the membrane to generate an open-circuit voltage of approximately 140 mV under mechanical stimulation confirms its potential as a

piezoelectric nanogenerator. These results suggest that PVDF/ZnO composites are promising materials for self-powered catalytic systems, offering a sustainable approach to environmental remediation and energy conversion. Future research should focus on optimizing the material's structure, exploring other pollutants, and integrating this system into real-world water treatment technologies.

Supplementary materials

No supplementary materials are available.

Data availability statement

Data will be made available on request.

Acknowledgments

This research was financially supported by the Russian Science Foundation No.22-73-10091.

Author contributions

Conceptualization: F.O., D.S.
Data curation: D.A.S., R.S.
Formal Analysis: F.O., D.S., A.M.
Funding acquisition: F.O.
Investigation: D.A.S., R.S., A.S., R.G., A.R., A.M.
Methodology: F.O., D.S.
Project administration: F.O.
Resources: F.O., D.S.
Software: A.M., A.R.
Supervision: F.O., D.S.
Validation: D.A.S., A.M.
Visualization: D.A.S., F.O., R.S.
Writing – original draft: D.A.S., F.O.
Writing – review & editing: F.O.

Conflict of interest

The authors declare no conflict of interest.

Additional information

Author IDs:

Daud Selimov, Scopus ID [57292170300](https://orcid.org/0000-0001-5729-2170),
Dinara Sobola, Scopus ID [57189064262](https://orcid.org/0000-0001-5718-9064),
Abdulatip Shuaibov, Scopus ID [57291948700](https://orcid.org/0000-0001-5729-1948),
Richard Schubert, Scopus ID [59326635900](https://orcid.org/0000-0001-5932-6635),
Rashid Gulakhmedov, Scopus ID [57291948600](https://orcid.org/0000-0001-5729-1948),
Alina Rabadanova, Scopus ID [57213688044](https://orcid.org/0000-0001-5721-3688),
Asiyat Magomedova, Scopus ID [57219780739](https://orcid.org/0000-0001-5721-9780),
Farid Orudzhev, Scopus ID [57201133063](https://orcid.org/0000-0001-5720-1133)

Websites:

Dagestan State University, <https://dgu.ru/>;
Brno University of Technology, <https://www.vut.cz/en/>;
Amirkhanov Institute of Physics of Dagestan Federal Research Center, Russian Academy of Sciences, <https://dagphys.su/>.

References

- Jiang B, Xue X, Mu Z, Zhang H, Li F, Liu K, Wang W, Zhang Y, Li W, Yang C, Zhang K. Contact-Piezoelectric Bi-Catalysis of an Electrospun ZnO@PVDF Composite Membrane for Dye Decomposition. *Molecules*. 2022;27:8579. doi:10.3390/MOLECULES27238579
- Zhang Y, Zhang X, Zhang Y, Zhang Y, Li H, Huang H. Enhanced piezo-photocatalytic activity of ZnS/Fe₂O₃: Benefit from type I junction and weak water flow-induced piezoelectric polarization. *J Photochem Photobiol A Chem*. 2025;460:116117. doi:10.1016/J.JPHOTOCHEM.2024.116117
- Xu Z, Wang J, Cai H, Li T, Chen F, Tu S, Huang H, Xu X Efficient photocatalytic and piezocatalytic performance in oxygen-vacant CdBiO₂Br with localized internal electric field. *Separation Purification Technol*. 2025;361:131460. doi:10.1016/J.SEPPUR.2025.131460
- Chandrasekar J, Venkatesan M, Hsu YC, Syu ZS, Chen WW, Hsu YF, Chung MA, Chen QG, Lee WY, Lin JH, Zhou Y, Kuo CC. In-situ oxidized MXene dopes for enhanced sensitivity of PVDF piezoelectric nanogenerators in Morse code transmission and photocatalysis applications. *Mater Today Energy*. 2025;48:101760. doi:10.1016/J.MTENER.2024.101760
- Liu Y, Chen T, Zheng J, Zhu Z, Huang Z, Hu C, Liu B. Enhanced piezo-catalytic performance of BaTiO₃ nanorods combining highly exposed active crystalline facets and superior deformation capability: Water purification and activation mechanism. *Chem Eng J*. 2024;488:150768. doi:10.1016/J.CEJ.2024.150768
- Li L, Lu S, Cao W, Zhu Q, Li R, Wei Y, Yang S, Wang C. Band Gap Engineering and Lattice Distortion for Synergetic Tuning Optical Properties of NaNbO₃ toward Enhanced Piezo-photocatalytic Activity. *Inorg Chem*. 2024;63:11745–11756. doi:10.1021/acs.inorgchem.4c01306
- Rabadanova AA, Selimov DA, Shuaibov AO, Alikhanov NM-R, Suleymanov SI, Shishov AY, Salnikov VD, Sangamesha MA, Giraev KM, Bamatov IM, Orudzhev FF. Smart multi-stimuli responsive magneto-piezoelectric composite material based on PVDF and BiFeO₃ nanoparticles for catalysis and energy harvesting. *Polymer* 2025;324:128241. doi:10.1016/J.POLYMER.2025.128241
- Li J, Li J, Yuan H, Sun X. Fabrication and catalytic activities of ZnSnO₃/C nanofibers in the piezo/photocatalysis of diclofenac. *Ceram Int*. 2024;50:33581–33589. doi:10.1016/J.CERAMINT.2024.06.174
- Zou X, Lu M, Yang H, Wu X. Novel MoS₂-based heterojunction as an efficient and magnetically retrievable piezo-photocatalyst for diclofenac sodium degradation. *Mater Today Sustainabil*. 2024;28:101000. doi:10.1016/J.MTSUST.2024.101000
- Zhang M, Nie S, Cheng T, Feng Y, Zhang C, Zheng L, Wu L, Hao W, Ding Y. Enhancing the macroscopic polarization of CdS for piezo-photocatalytic water splitting. *Nano Energy*. 2021;90:106635. doi:10.1016/J.NANOEN.2021.106635
- Li M, Liu L, Li Y, Li Y. Tuning piezoelectric driven photocatalysis by TiO₂/ZnS heterojunction for mineral processing wastewater degradation. *J Water Process Eng*. 2024;64:105727. doi:10.1016/J.JWPE.2024.105727
- Bettini S, Pagano R, Valli D, Inghrosso C, Roeffaers M, Hofkens J, Giancane G, Valli L. ZnO nanostructures based piezo-photocatalytic degradation enhancement of steroid hormones. *Surfaces Interfaces*. 2023;36:102581. doi:10.1016/J.SURFIN.2022.102581
- Borysiewicz MA. ZnO as a functional material, a review. *Crystals*. 2019;9:505. doi:10.3390/CRYST9100505
- Consonni V, Lord AM. Polarity in ZnO nanowires: A critical issue for piezotronic and piezoelectric devices. *Nano Energy*. 2021;83:105789. doi:10.1016/J.NANOEN.2021.105789
- Xu X, Jia Y, Xiao L, Wu Z. Strong vibration-catalysis of ZnO nanorods for dye wastewater decolorization via piezo-electro-chemical coupling. *Chemosphere*. 2018;193:1143–1148. doi:10.1016/J.CHEMOSPHERE.2017.11.116
- Nie Q, Xie Y, Ma J, Wang J, Zhang G. High piezo-catalytic activity of ZnO/Al₂O₃ nanosheets utilizing ultrasonic energy for wastewater treatment. *J Cleaner Production*. 2020;242:118532. doi:10.1016/J.JCLEPRO.2019.118532
- Truong Hoang Q, Ravichandran V, Nguyen Cao TG, Kang JH, Ko YT, Lee T II, Shim MS. Piezoelectric Au-decorated ZnO nanorods: Ultrasound-triggered generation of ROS for piezocatalytic cancer therapy. *Chem Eng J*. 2022;35:135039. doi:10.1016/J.CEJ.2022.135039
- Zhang Q, Jia Y, Chen J, Wang X, Zhang L, Chen Z, Wu Z. Strongly enhanced piezocatalysis of BiFeO₃/ZnO heterostructure nanomaterials. *New J Chem*. 2023;47:3471–3480. doi:10.1039/D2NJ05732H
- Ma W, Lv M, Cao F, Fang Z, Feng Y, Zhang G, Yang Y, Liu H. Synthesis and characterization of ZnO-GO composites with their piezoelectric catalytic and antibacterial properties. *J Environ Chem Eng*. 2022;10:107840. doi:10.1016/J.JECE.2022.107840
- Magomedova AG, Rabadanova AA, Shuaibov AO, Selimov DA, Sobola DS, Rabadanov KS, Giraev KM, Orudzhev FF. Combination NIPS/TIPS Synthesis of α-Fe₂O₃ and α/γ-Fe₂O₃ Doped PVDF Composite for Efficient Piezocatalytic Degradation of Rhodamine B. *Molecules*. 2023;28:6932. doi:10.3390/MOLECULES28196932/S1
- Ding J, Han Z, Yang X, Liu J, Guo K, Fan H, Hu P, Teng F. Multifunctional ZnO/PVDF hybrid fiber membrane: Enhanced photocatalytic degradation performance and oil/water separation application. *Mater Sci Semiconductor Processing*. 2025;185:108942. doi:10.1016/J.MSSP.2024.108942
- Li Q, Lin R, Tang Z, Liang S, Xue X, Xing L (2024) A flexible self-cleaning/antibacterial PVDF/T-ZnO fabric based on piezo-photocatalytic coupling effect for smart mask. *J Phys D Appl Phys*. 2024;57:305106. doi:10.1088/1361-6463/AD4368
- Postica V, Vahl A, Santos-Carballal D, Dankwort T, Kienle L, Hoppe M, Cadi-Essadek A, De Leeuw NH, Terasa MI, Adelung R, Faupel F, Lupan O Tuning ZnO Sensors Reactivity toward Volatile Organic Compounds via Ag Doping and Nanoparticle Functionalization. *ACS Appl Mater Interfaces*. 2019;11:31452–31466. doi:10.1021/acsami.9b07275
- Xu D, Fan D, Shen W. Catalyst-free direct vapor-phase growth of Zn_{1-x}Cu_xO micro-cross structures and their optical properties. *Nanoscale Res Lett*. 2013;8:1–9. doi:10.1186/1556-276X-8-46
- Jin Y, Cui Q, Wen G, Wang Q, Hao J, Wang S, Zhang J. XPS and Raman scattering studies of room temperature ferromagnetic ZnO : Cu. *J Phys D Appl Phys*. 2009;42:215007. doi:10.1088/0022-3727/42/21/215007
- Ma W, Xu L, Tian Z, Zang A; Changes in photocatalytic activity and optical properties of ZnO whiskers induced by UV irradiation. *J Luminescence*. 2022;249:119015. doi:10.1016/J.JLUMIN.2022.119015
- Pandey P, Parra MR, Haque FZ, Kurchania R. Effects of annealing temperature optimization on the efficiency of ZnO nanoparticles photoanode based dye sensitized solar cells. *J Mater Sci Mater Electronics*. 2017;28:1537–1545. doi:10.1007/S10854-016-5693-9
- Filippov S, Wang XJ, Devika M, Koteeswara Reddy N, Tu CW, Chen WM, Buyanova IA. Effects of Ni-coating on ZnO nanowires: A Raman scattering study. *J Appl Phys*. 2013;113: doi:10.1063/1.4807912/371284
- Yang AL, Wei HY, Liu XL, Song HP, Fan HB, Zhang PF, Zheng GL, Yang SY, Zhu QS, Wang ZG. Characterization of ZnMgO hexagonal-nanotowers/films on m-plane sapphire synthesized by metal organic chemical vapour deposition. *Journal of Phys D Appl Phys*. 2008;41:205416. doi:10.1088/0022-3727/41/20/205416
- Nizar BM, Lajnef M, Chaste J, Chtourou R, Herth E. Highly C-oriented (002) plane ZnO nanowires synthesis. *RSC advances* 2023;13:15077–15085. doi:10.1039/D3RA01511D
- Chassaing PM, Demangeot F, Paillard V, Zwick A, Combe N, Paës C, Kahn ML, Maisonnat A, Chaudret B. Raman study of E₂ and surface phonon in zinc oxide nanoparticles

- surrounded by organic molecules. *Appl Phys Lett*. 2007;91: doi:[10.1063/1.2757591/167774](https://doi.org/10.1063/1.2757591/167774)
32. Sliem MA, Hikov T, Li ZA, Spasova M, Farle M, Schmidt DA, Havenith-Newen M, Fischer RA. Interfacial Cu/ZnO contact by selective photodeposition of copper onto the surface of small ZnO nanoparticles in non-aqueous colloidal solution. *Phys Chem Chem Phys*. 2010;12:9858–9866. doi:[10.1039/C003861J](https://doi.org/10.1039/C003861J)
33. Orudzhev F, Selimov D, Rabadanova A, Shuaibov A, Abdurakhmanov M, Gulakhmedov R, Papež N, Ramazanov S, Zvereva I, Částková K (2023) 1D/2D Electrospun Polyvinylidene Fluoride Nanofibers/Carbon Flakes Hybrid Nonmetal Polymeric Photo- and Piezocatalyst. *ChemistrySelect*. 2023;8:e202303318. doi:[10.1002/SLCT.202303318](https://doi.org/10.1002/SLCT.202303318)
34. Purushothaman SM, Tronco MF, Ponçot M, Chitralkha CS, Guigo N, Malfois M, Kalarikkal N, Thomas S, Royaud I, Rouxel D. Quantifying the Crystalline Polymorphism in PVDF: Comparative Criteria Using DSC, WAXS, FT-IR, and Raman Spectroscopy. *ACS Appl Polymer Mater*. 2024;6:8291–8305. doi:[10.1021/acscapm.4c01157](https://doi.org/10.1021/acscapm.4c01157)
35. Khan F, Kowalchik T, Roundy S, Warren R. Stretching-induced phase transitions in barium titanate-poly(vinylidene fluoride) flexible composite piezoelectric films. *Scripta Materialia*. 2021;193:64–70. doi:[10.1016/j.scriptamat.2020.10.036](https://doi.org/10.1016/j.scriptamat.2020.10.036)
36. Selimov DA, Rabadanova AA, Shuaibov AO, Magomedova AG, Abdurakhmanov MG, Gulakhmedov RR, Ramazanov SM, Amirov AA, Sobola DS, Orudzhev FF. Piezo-Enhanced Photocatalytic Activity of BaTiO₃-Doped Polyvinylidene Fluoride Nanofibers. *Kinetics Catalysis*. 2024;65:682–694. doi:[10.1134/S0023158424602407](https://doi.org/10.1134/S0023158424602407)
37. Bridelli MG, Bridelli MG (2017) Fourier Transform Infrared Spectroscopy in the Study of Hydrated Biological Macromolecules. *Fourier Transforms - High-tech Application and Current Trends*. doi:[10.5772/66576](https://doi.org/10.5772/66576)
38. Orudzhev FF, Sobola DS, Ramazanov SM, Částková K, Selimov DA, Rabadanova AA, Shuaibov AO, Gulakhmedov RR, Abdurakhmanov MG, Giraev KM. Hydrogen Bond-Induced Activation of Photocatalytic and Piezophotocatalytic Properties in Calcium Nitrate Doped Electrospun PVDF Fibers. *Polymers*. 2023;15:3252. doi:[10.3390/POLYM15153252](https://doi.org/10.3390/POLYM15153252)
39. Gregorio R. Determination of the α , β , and γ crystalline phases of poly(vinylidene fluoride) films prepared at different conditions. *J Appl Polymer Sci*. 2006;100:3272–3279. doi:[10.1002/APP.23137](https://doi.org/10.1002/APP.23137)
40. Rabadanova A, Abdurakhmanov M, Gulakhmedov R, Shuaibov A, Selimov D, Sobola D, Částková K, Ramazanov S, Orudzhev F. Piezo-, photo- and piezophotocatalytic activity of electrospun fibrous PVDF/CTAB membrane. *Chimica Techno Acta*. 2022;9:20229420. doi:[10.15826/chimtech.2022.9.4.20](https://doi.org/10.15826/chimtech.2022.9.4.20)
41. Simanjuntak FM, Ohno T, Samukawa S. Neutral Oxygen Beam Treated ZnO-Based Resistive Switching Memory Device. *ACS Appl Electronic Mater*. 2019;1:18–24. doi:[10.1021/acsaelm.8b00055](https://doi.org/10.1021/acsaelm.8b00055)
42. Kim W, Choi M, Yong K. Generation of oxygen vacancies in ZnO nanorods/films and their effects on gas sensing properties. *Sensors Actuators B Chem*. 2015;209:989–996. doi:[10.1016/j.SNB.2014.12.072](https://doi.org/10.1016/j.SNB.2014.12.072)
43. Singh P, Simanjuntak FM, Wu YC, Kumar A, Zan HW, Tseng TY. Sensing performance of gas sensors fabricated from controllably grown ZnO-based nanorods on seed layers. *J Mater Sci*. 2020;55:8850–8860. doi:[10.1007/s10853-020-04659-7](https://doi.org/10.1007/s10853-020-04659-7)
44. Orudzhev F, Muslimov A, Selimov D, Gulakhmedov RR, Lavrikov A, Kanevsky V, Gasimov R, Krasnova V, Sobola D. Oxygen Vacancies and Surface Wettability: Key Factors in Activating and Enhancing the Solar Photocatalytic Activity of ZnO Tetrapods. *Int J Molecular Sci*. 2023;24:16338. doi:[10.3390/IJMS242216338](https://doi.org/10.3390/IJMS242216338)
45. Wei Y, Zhang Y, Geng W, Su H, Long M. Efficient bifunctional piezocatalysis of Au/BiVO₄ for simultaneous removal of 4-chlorophenol and Cr(VI) in water. *Applied Catalysis B: Environment*. 2019;259:118084. doi:[10.1016/j.APCATB.2019.118084](https://doi.org/10.1016/j.APCATB.2019.118084)
46. Wu J, Xu Q, Lin E, Yuan B, Qin N, Thatikonda SK, Bao D. Insights into the Role of Ferroelectric Polarization in Piezocatalysis of Nanocrystalline BaTiO₃. *ACS Appl Mater Interfaces* 2018;10:17842–17849. doi:[10.1021/acscami.8b01991](https://doi.org/10.1021/acscami.8b01991)
47. Li S, Zhao Z, Yu D, Zhao JZ, Su Y, Liu Y, Lin Y, Liu W, Xu H, Zhang Z. Few-layer transition metal dichalcogenides (MoS₂, WS₂, and WSe₂) for water splitting and degradation of organic pollutants: Understanding the piezocatalytic effect. *Nano Energy*. 2019;66:104083. doi:[10.1016/j.NANOEN.2019.104083](https://doi.org/10.1016/j.NANOEN.2019.104083)
48. Domingo N. Understanding piezocatalysis, pyrocatalysis and ferrocatalysis. *Frontiers Nanotechnol*. 2024;6:1320503. doi:[10.3389/FNANO.2024.1320503](https://doi.org/10.3389/FNANO.2024.1320503)